ACS Energy LETTERS

http://pubs.acs.org/journal/aelccp

LETTER

SMART Perovskite Growth: Enabling a Larger Range of Process Conditions

Chuanxiao Xiao,[†] Fei Zhang,*[,†] Xihan Chen,[†] Mengjin Yang, Steven P. Harvey, Matthew C. Beard, Joseph J. Berry, Chun-Sheng Jiang,* Mowafak M. Al-Jassim, and Kai Zhu*

Cite This: https://dx.doi.org/10.1021/acsenergylett.0c02578

Read Online

ACCESS | Metrics & More | Article Recommendations | Supporting Information

ABSTRACT: Cost-effective, high-throughput industrial applications of metal-halide perovskites require a highly tolerant method (i.e., wide process window) that produces high-quality materials with a short annealing time. Here, we introduce a Seed Modulation for ARTificially controlled nucleation (SMART) process that enables rapid fabrication of high-quality perovskite films under a wide set of initial input parameters. We characterized the thin-film evolution from the perspective of crystallinity, surface potential, diffusivity, surface carrier dynamics, and interfacial recombination. We find that surface and subsurface defects primarily determine the performance of materials and devices. By modulating the seeds for perovskite nucleation, we were able to improve the overall crystallization. We achieved a >20% power conversion efficiency using only a 5 min annealing step, and we found that the annealing window is widened such that differing initial conditions achieve similar quality. Furthermore, we demonstrated reproducibility and performance improvement in larger-area perovskite cells by incorporating the SMART process.

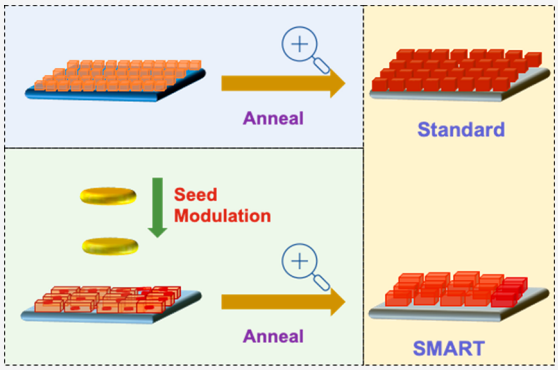

Thanks to an intensive worldwide effort, hybrid organic−inorganic metal-halide perovskite-based solar cells have rapidly reached remarkable certified power conversion efficiencies of up to 25.5%.[1] Metal-halide perovskite semiconductors possess many remarkable properties suitable for optoelectronic applications, such as strong optical absorption, low exciton-binding energy, long charge-carrier lifetimes, and performance characteristics that are highly defect-tolerant with low nonradiative recombination rates.[2−11] Currently, to fabricate the state-of-the-art devices and within most academic laboratories, a simple solution-processing method is widely employed. However, solution-processing involves a complicated set of interconnected processes that include the deposition of a wet precursor onto a substrate, solvent evaporation, crystal nucleation, formation of the perovskite phase or an intermediate solid phase, and crystallization. These processes often overlap with each other, which complicates the perovskite microstructure evolution.[12,13] Small initial variations can significantly alter the final film properties because they enable differing film-growth mechanisms and microstructure formation pathways.[2,14−17] This complicated nature of solution-coated perovskite thin films results in narrow processing windows to acquire high-quality materials, which makes it difficult to replicate results from different laboratories, and it will ultimately hinder large-scale fabrication endeavors.[18−21] On the other hand, annealing is a necessary step to transfer the wet precursor film into a solid-state perovskite film, promote crystal growth, and reduce defect density by excluding impurities. Annealing times for typical perovskite films are from 30−60 min at a temperature of 100−150 °C;[22−26] note that a long annealing time is not necessary, and it is possible to make high efficiency perovskite solar cells rapidly.[27−30] A shortened annealing time at lower temperature is highly preferred for cost-effective, high-throughput industrial applications. Thus, the perovskite community needs to develop a facile reproducible method for high-quality perovskite materials' fabrication with a short annealing time and a wide process window, as well as a deeper understanding of the perovskite film formation and the correlation of process input parameters to output performance characteristics.

Inspired by the cast-mono silicon growth method, we advance a simple, yet general, seed-assisted method to grow

Received: December 13, 2020
Accepted: January 19, 2021

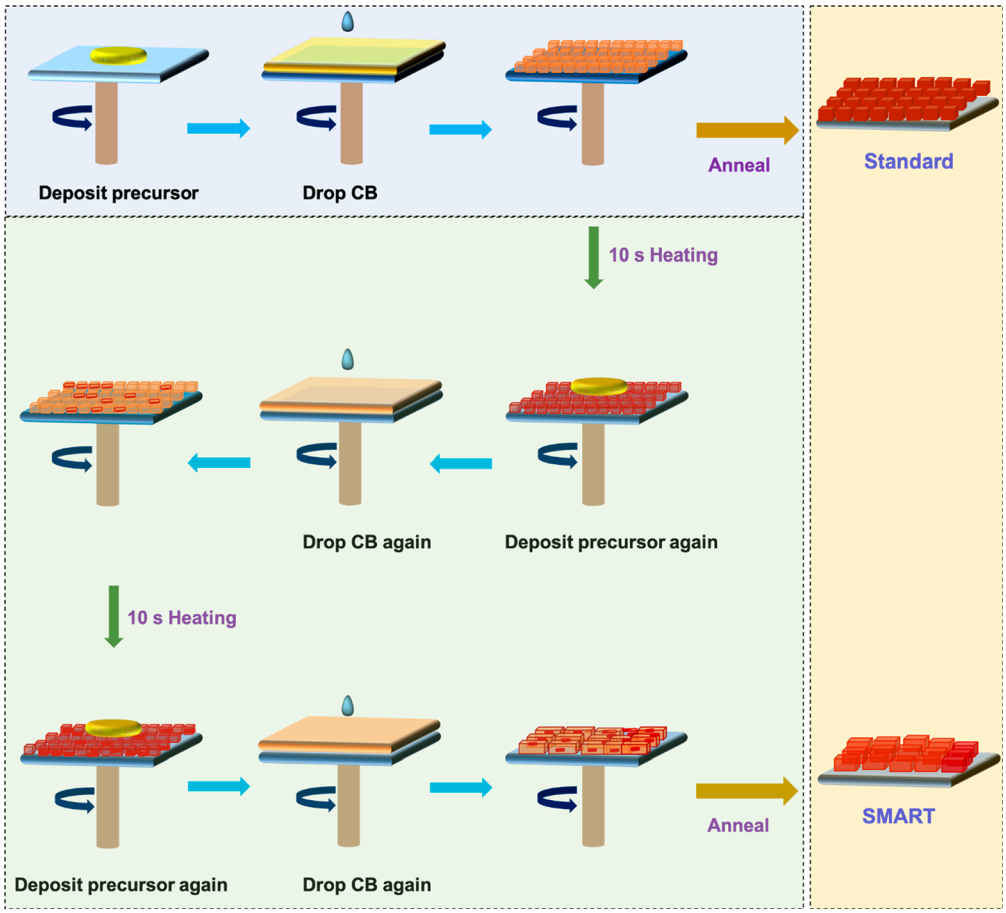

Figure 1. Schematic of standard and SMART process for depositing perovskite film. Note: CB = chlorobenzene.

high-quality metal-halide perovskite thin films, enabling fast crystallization and a widened annealing window. The cast-mono process is a novel technique to rapidly grow quasi-single-crystalline (sc) silicon,[31,32] where the resulting multicrystalline (mc) silicon has fewer grain boundaries and dislocations, especially at the bottom and middle regions of the ingots. Such wafers can exhibit about a 1.0% absolute efficiency improvement compared with conventional mc-silicon wafers. Instead of the slow and expensive Czochralski (CZ) process to manufacture monocrystalline silicon ingots, the high-throughput cast-mono process uses a <100>-oriented single crystal as a seed at the bottom of the crucible; the silicon ingot solidifies mimicking the crystal orientation of the seed wafer under careful control of a vertical temperature gradient in the furnace. The single silicon crystal seed is vital for the cast-mono process. In the perovskite growth method developed here, we obtained high-quality seeds by dissolving the precursor film, which is a hypothesis consistent with other published reports.[33,34] In this work, a wet precursor film is first spin-coated onto a substrate, followed by the chlorobenzene (CB) antisolvent method, then briefly heating the film for 10 s; after which, we spin-coat the same precursor ink on top of the sample and repeat the procedure twice. After the 10-s heating, the film is slightly crystallized; the precursor ink dissolves the previous dried-precursor film. The twice-repeated deposition-dissolution process is assumed to leave some nuclei that are stable with a higher formation energy. The leftover material with the same perovskite elements can then act as heterogeneous nucleation sites, lowering the Gibbs free energy, which facilitates the subsequent metal-halide perovskite growth.[17,35] Finally, we anneal the sample, resulting in a high-quality perovskite thin film. This approach combines the conventional "one-step" perovskite deposition[2,17] and the key feature of seed crystals in the cast-mono silicon growth. We call this approach **S**eed **M**odulation for **ART**ificially controlled nucleation, or SMART. The schematic of the perovskite deposition process is shown in Figure 1. With the assistance of the seeds having high formation energy, the as-grown SMART perovskite thin film forms fewer defects; hence, the subsequent annealing time can be shorter and becomes less critical. We demonstrate that a >20% power conversion efficiency can be achieved by the SMART perovskite film processing with an annealing time as short as 5 min. We find that the annealing time can be between 5 and 60 min without a significant difference in performance characteristics. This flexible annealing time allows for higher reproducibility in producing similar high-quality perovskite materials, which is preferable for scaled-up manufacturing. Note that we demonstrate SMART mostly by spin-coating, but the approach is general and applicable for other solution-based methods, such as blade coating, slot-die coating, and spray coating, which may be more favorable for large-area fabrications.[19] We also demonstrated that the SMART method improves larger-area perovskite cells made by blade-coating, by simply using the spin-coated perovskite precursor without any optimization.

Understanding the mechanism that governs the film formation process can provide insights for further improving high-quality perovskite thin-film fabrication. In this work, we

https://dx.doi.org/10.1021/acsenergylett.0c02578
ACS Energy Lett. XXXX, XXX, XXX−XXX

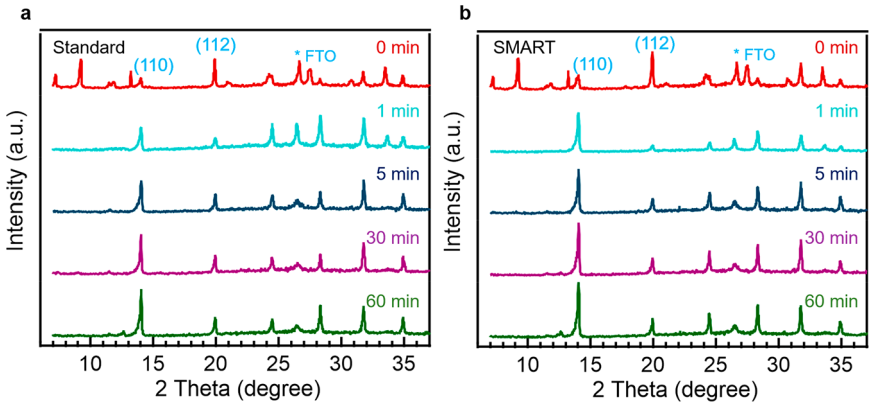

Figure 2. X-ray diffraction results of the perovskite films with different anneal time at 0, 1, 5, 30, and 60 min. (a) Patterns of standard films; (b) Patterns of SMART films.

characterized the evolution of a standard film and a SMART film during annealing, characterizing both fundamental materials' properties and resulting device performance. From these different perspectives, we measured crystallinity, surface potential, diffusivity, and surface charge-carrier recombination, and evaluated junction quality and interfacial recombination. The measurements correlate thin-film characteristics with device performance. Our results reveal that the improvements observed using the SMART perovskite thin-film deposition can be attributed to the resulting improved surface carrier dynamics. Also, the resultant perovskite film alters the interface recombination at the device level, which plays an important role in device performance. Further improved control of surface carrier dynamics should result in perovskite materials with even higher quality and lead to enhanced device performance.

We performed X-ray diffraction (XRD) to investigate the crystallinity and orientation of the standard and SMART perovskite thin film during annealing. The results are shown in Figure 2. The XRD patterns exhibited stronger and sharper perovskite characteristic peaks as we annealed the films. In particular, the (110) peak (2θ at ~14.0°) was greatly enhanced, with a reduced full width at half-maximum (fwhm) for both the standard and SMART perovskite thin films. The fwhm in these films are shown in Figure S1. The results indicate improved crystallization and clear texturing in the preferred (110) orientation in the resulting perovskite thin films, as (110) peak intensity increases and fwhm decreases after annealing. On the as-grown wet films, some peaks do not belong to the perovskite phase but rather can be associated with the solvent (e.g., 2θ<10°). For the standard film, the crystallinity gradually evolves during the 60 min process window, whereas the transformation to a high-quality perovskite material in the SMART thin films occurs much faster and with higher quality. The 0 min SMART thin film has a similar XRD pattern as the standard film but has a higher intensity of the (110) peak; however, the SMART film crystallized faster even at only 1 min and after annealing for 5 min, the peaks become comparable with that for the 30 min and 60 min standard thin films, as judged by (110) peak intensity and fwhm. The results support our hypothesis that the as-grown SMART perovskite materials, which initiate high-quality seeds, are less defective, and the annealing time is less critical in producing a high-quality crystalline perovskite phase. The majority of grains exhibit a preferred (110) orientation, suggesting that the seeds in the SMART process may be dominated by the (110) orientation with the smallest surface energy. Further annealing continues to slightly increase the XRD peak intensities and lowers their fwhm. The improved crystallinity results in a decrease in nonradiative recombination through charge-carrier trap states. Thus, the SMART films evolve faster and yield higher-quality thin films with fewer deleterious defects (i.e., those that impact carrier lifetimes). The same results were also confirmed by 2D XRD, as shown in Figure S2. The XRD results show that the crystalline perovskite phase forms more quickly during the annealing step for the SMART films than for the standard films. The defect density may also be controlled with the different nucleation process inherent in the SMART procedure. In the SMART process, the perovskite seeds left on the substrate may effectively lower the Gibbs free energy that governs crystal growth; the kinetic barrier is smaller for a grain growing on existing nuclei, and it therefore results in a less defective precursor film. We also performed time-of-flight secondary-ion mass spectrometry (TOF-SIMS) on the films and found the SMART 0 min film has substantially higher ratio of Pb^+, I^-, and Br^-. The different chemical ratio could alter defect density and also the crystallization process (Figure S3). SMART process appears to improve the grain size and facilitate perovskite growth with perpendicular orientation to the substrate according to the cross-sectional SEM images (Figure S4), which is consistent with the results of XRD.

We examined the surface potential and topography by scanning Kelvin probe force microscopy (KPFM), to show evidence of the existence of the seeds (Figure S5). We prepared two samples: 1. pristine TiO_2 after DMSO/DMF rinsing; 2. a TiO_2 substrate that we deposited in the SMART perovskite and then washed away by the same amount of DMSO/DMF as used in perovskite deposition. We found the roughness of the SMART-treated sample decreases from 36.7 to 27.3 nm, suggesting additional materials deposited on the substrate (may first be filled on the lower area on the TiO_2 mesoporous structure). Furthermore, the corresponding KPFM images show that ~400 mV higher surface potential in the SMART-treated sample. The substantial change of work function indicates that some materials have remained on the TiO_2 surface, which we hypothesize provide seeds for subsequent perovskite crystallization. TOF-SIMS also clearly showed that the key elements of the perovskite components (e.g., CH_5N_2, Pb, Cs) are left on the substrate (Figure S6), which is consistent with the KPFM results. However, we cannot confirm the exact composition of the seeds by a few

https://dx.doi.org/10.1021/acsenergylett.0c02578
ACS Energy Lett. XXXX, XXX, XXX−XXX

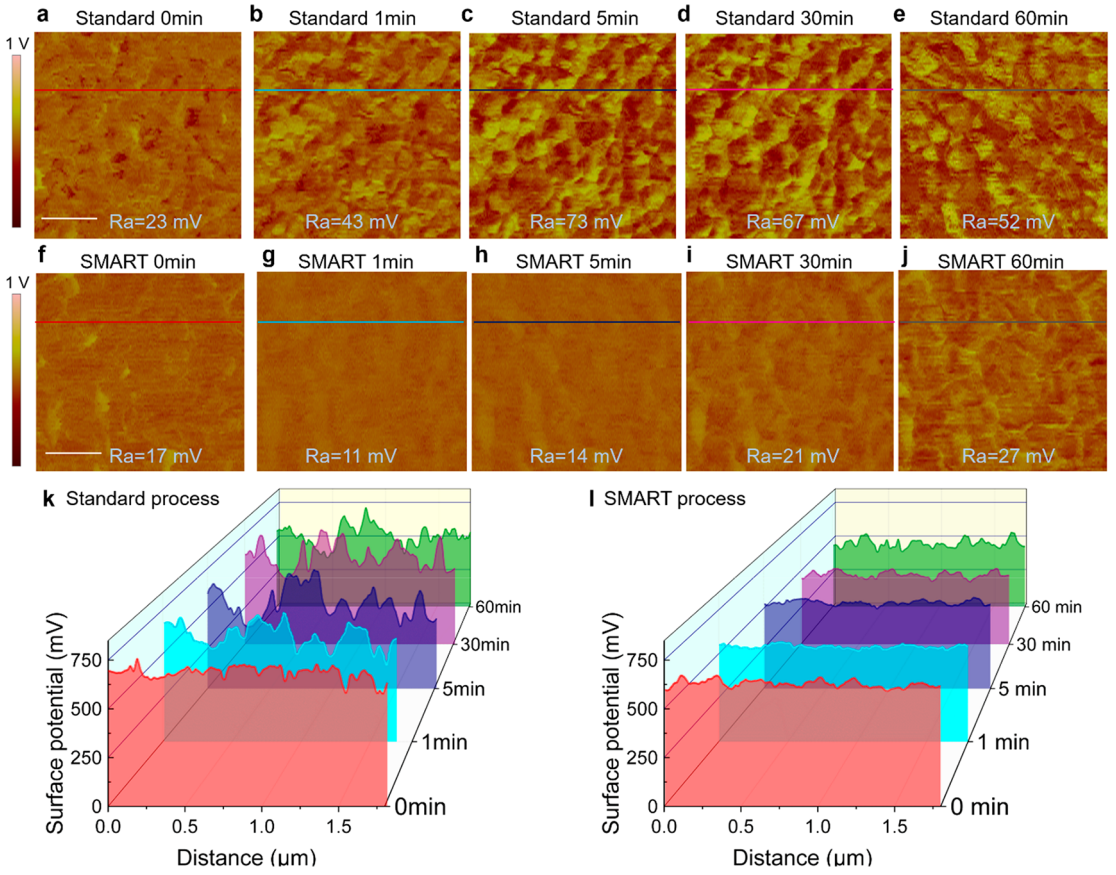

Figure 3. In situ KPFM mappings of standard and SMART films under different annealing time. (a−e) Surface-potential mapping of standard film without annealing, with 1, 5, 30, and 60 min annealing on the same location, respectively; (f−j) Surface-potential mapping of SMART film without annealing, with 1, 5, 30, and 60 min annealing on the same location, respectively; Scale bar: 500 nm. (k,l) Surface-potential line profiles of standard and SMART samples under different annealing times.

standard techniques (e.g., XRD and photoluminescence), which is likely due to the amount of residual/seed materials is below the detection limit of these techniques.

We monitored the surface potential evolution of the films during annealing by in situ KPFM.[36] The KPFM scans start from a precursor film without annealing, and then the KPFM is performed on the same location after the annealing. Figure 3 shows the surface-potential images of the standard and SMART films with annealing times of 0, 1, 5, 30, and 60 min and correspond to the XRD-characterized films. Note that the film topography changes slightly during annealing, but we are still able to identify the same region for the KPFM (see Figures S7, S8). Note that even the same average topography, morphology, or grain size can have significantly different electrical properties (i.e., the surface potential is not dominated by surface morphology).

KPFM measures a contact-potential difference between the tip and sample; the sample surface work function is calculated by subtracting the measured surface-potential value from the work function of the tip. In the XRD measurements, the perovskite structure forms in the first 1 min annealing period. After 5 min, the potential did not change too much for the SMART samples; therefore, the 0−5 min surface-potential evolution should reflect a bulk change. We observe a decrease in surface potential when comparing the 0 min and 5 min films for both the standard and SMART samples. The decreased surface potential indicates an increase in the work function, where the films move toward *p*-type or less *n*-type behavior,[37] and it is consistent with the appearance of the perovskite phase in XRD patterns.

The XRD results of further-annealed standard films at 30 and 60 min show similar patterns without the addition of new peaks, suggesting that the quality of the perovskite film is improved with higher crystallinity and fewer defects for longer anneal times. The change in the defect states can be resolved by the KPFM surface-potential mapping. We note the roughness information on potential images in Figure 3m and the potential distribution histogram in Figure S9. With the prolonged annealing time, the surface-potential fluctuation becomes smaller in the standard sample set. The potential distribution in Figure 3b−e is not uniform, with fluctuations occurring mainly between different morphological domain interiors, which suggests the presence of a high density of surface and/or subsurface defects. In addition to surface defects, the subsurface area may contain charged defects such as V_I (iodine vacancy) and Pb_I (I-site substitution y Pb) because density functional theory (DFT)-calculated defect formation energies are low for these defects.[38] These gap states at the surface and subsurface regions should have a deterministic effect on Shockley−Read−Hall recombination events. In contrast, the SMART samples showed less dramatic changes in surface potential (Figure 3g−j). Upon further annealing during the SMART process, the potential roughness slightly increases because of a higher surface potential at domain boundaries, whereas the domain interiors have a similar potential. A higher surface potential indicates down-

https://dx.doi.org/10.1021/acsenergylett.0c02578
ACS Energy Lett. XXXX, XXX, XXX−XXX

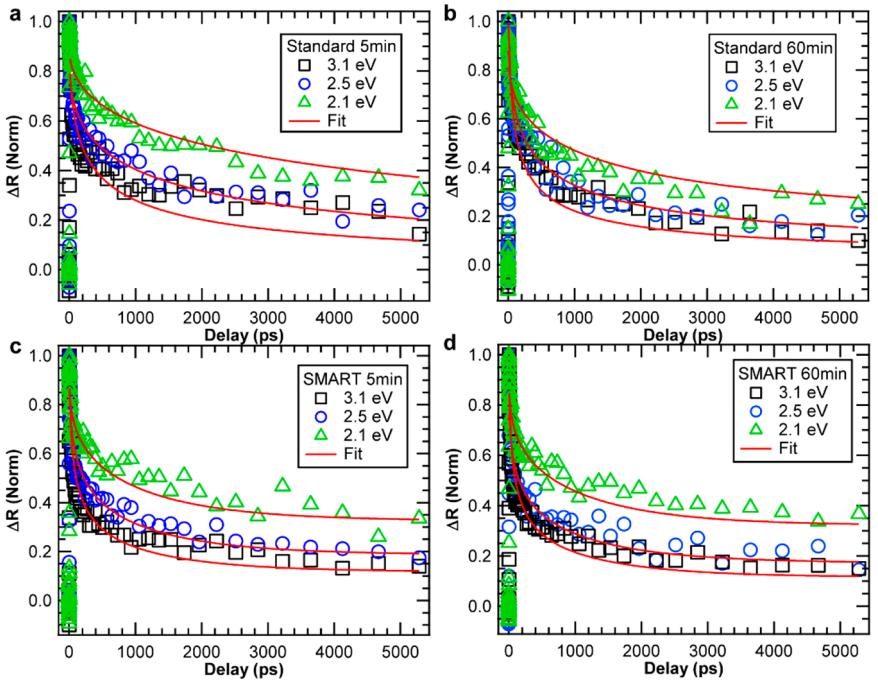

Figure 4. Kinetics measured with transient reflectance spectroscopy at 3.1, 2.5, and 2.1 eV pump energy for standard perovskite thin films with (a) 5 min and (b) 60 min annealing. Transient kinetics for SMART perovskite thin films with (c) 5 min and (d) 60 min annealing. The red solid lines are nonlinear least-squares global best-fit curves using fitting methods described in the main text. The ambipolar carrier diffusion coefficient, *D*, and surface recombination velocity (SRV; denoted as *S*) determined from the global fittings are summarized in Table 1.

ward band-bending around the domain boundaries, where electrons (minority carriers) are attracted toward these regions and holes (majority carriers) are repulsed.[39,40] The in situ KPFM mapping reveals that surface and subsurface defects are different in standard and SMART processes. In the SMART process, it is reasonable that the seeded growth leads to formation of an improved crystalline material with fewer grains, and the surface defects are suppressed when compared with the standard process.

To further understand the effect of crystal formation processes and the resulting change in surface potential on photogenerated carriers, we used transient reflection spectroscopy to investigate the surface carrier dynamics (Figure 4, Figure S10). The perovskite phase forms after 5 min of annealing, so we focus on the film after 5 min of annealing. Figure 4a–d illustrates the surface carrier dynamics at different excitation energies with different heating conditions for the standard and SMART thin films. Figure 4a,b plots the kinetics for the standard film at 5- and 60 min heating when photoexciting with 3.1, 2.5, and 2.1 eV. The major contribution to the observed kinetics is carrier diffusion and surface recombination; therefore, the kinetics can be modeled with the following set of equations:

$$\frac{\partial N(x,t)}{\partial t} = D\frac{\partial^2 N(x,t)}{\partial x^2} - \frac{N(x,t)}{\tau_B} \quad (1)$$

$$N(x,0) = N_0 \cdot \exp(-\alpha x) \quad (2)$$

$$\frac{\partial N(x,t)}{\partial t}\Big|_{x=0} = \frac{S_F}{D} N(0,t) \quad (3)$$

$$\frac{\partial N(x,t)}{\partial t}\Big|_{x=L} = -\frac{S_B}{D} N(L,t) \quad (4)$$

where D is the ambipolar diffusion constant, α is the absorption coefficient determined from ellipsometry, L is the thickness of the polycrystalline thin film (0.65 μm), and S_F and S_B are the surface recombination velocities (SRVs) for the front and back surfaces, respectively. For the standard films, the data reveal a factor of 3 increase in the extracted diffusion coefficient, whereas the SRV decreases slightly, comparing the 60 min heating vs 5 min annealing times. Figure 4c,d plots the kinetics for SMART samples annealed for 5 and 60 min, respectively. We apply the same modeling as described above and find only minor changes in the extracted D and SRV between these samples. In addition, SMART-treated films exhibit a 4×-lower SRV and a 2×-higher diffusion coefficient vs the standard films, which is consistent with the surface-potential measurements from in situ KPFM—that is, the surface-potential variations change significantly for the standard film during annealing but only slightly for the SMART films (except for the boundary regions, where we observed KPFM potential variations). The extracted D and SRV values are listed in Table 1. The total carrier lifetime of the films was also investigated, and the data are summarized in the Supporting Information. From the total carrier-lifetime measurements, the diffusion length of carriers can be obtained

Table 1. Fitted Ambipolar Diffusion Coefficient, Surface Recombination Velocity (SRV), and Calculated Diffusion Length for Standard and SMART Perovskite Thin Films

thin film	D (cm^2/s)	SRV (cm/s)	diffusion length (μm)
standard 5 min	0.05 ± 0.006	540 ± 40	1.0 ± 0.1
standard 60 min	0.17 ± 0.01	480 ± 60	1.4 ± 0.1
SMART 5 min	0.35 ± 0.03	130 ± 20	2.2 ± 0.1
SMART 60 min	0.35 ± 0.04	100 ± 30	2.2 ± 0.1

https://dx.doi.org/10.1021/acsenergylett.0c02578
ACS Energy Lett. XXXX, XXX, XXX−XXX

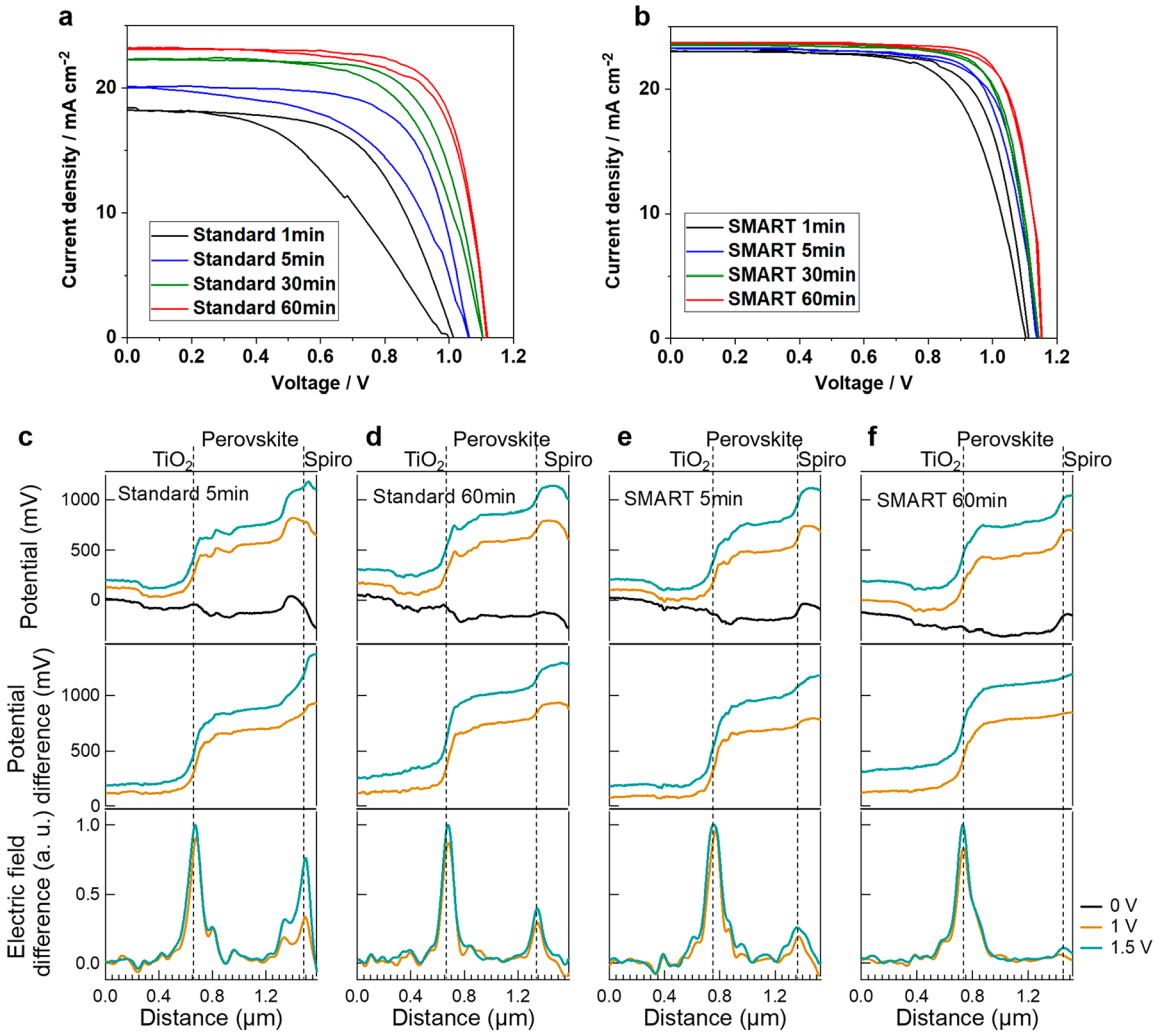

Figure 5. (a,b) Device performance of perovskite solar cells; (c–f) Results of KPFM electrical potential and field profiling on the cross-sectional surface of perovskite solar cells. Top: Potential profile under 0, −1, and −1.5 V bias voltages; Middle: Potential difference between the various applied bias voltages and 0 V; Bottom: Change in electric field; the curves were calculated by taking the first derivatives of the potential difference.

as $L = \sqrt{D\tau}$ (see Table 1). From measurements of the surface carrier dynamics, we estimated that for the standard thin films, the diffusion length increases from 1 to 1.4 μm when the annealing time increases from 5 to 60 min. For the SMART thin films, the diffusion length reaches 2.2 μm after 5 min annealing and remains the same (2.2 μm) after a 60 min annealing step. With the SMART process, the carrier diffusion length increases by a factor of 2 compared to the standard film, but also, the annealing window is widened.

We fabricated two groups of devices with 1, 5, 30, and 60 min-annealing under the standard and SMART conditions, with the same cell architectures. The solar cells have a conventional mesoporous structure of glass/fluorine-doped tin oxide (FTO)/compact-TiO_2/mesoporous-TiO_2/perovskite/spiro-OMeTAD/Au, where TiO_2 is used as an electron-transport material (ETM), spiro-OMeTAD is used as a hole-transport material (HTM), and FTO and Au are electrodes. The device current density–voltage characteristics and the corresponding photovoltaic parameters are shown in Figure 5a,b and Table 2, respectively. We refer to the cells according to the perovskite films that were used in the devices; for

Table 2. Performance Parameters of Best Corresponding Perovskite-Based Solar Cells under Different Scan Directions

samples	scan direction	V_{oc} (V)	J_{sc} (mA/cm^2)	FF	PCE (%)
standard 1 min	forward	1.010	18.24	0.45	8.3
	backward	1.012	18.40	0.60	11.2
standard 5 min	forward	1.063	20.12	0.56	12.0
	backward	1.063	20.14	0.69	14.8
standard 30 min	forward	1.106	22.31	0.65	16.1
	backward	1.104	22.29	0.71	17.5
standard 60 min	forward	1.121	23.12	0.72	18.7
	backward	1.120	23.22	0.74	19.3
SMART 1 min	forward	1.101	23.05	0.70	17.8
	backward	1.109	23.10	0.73	18.7
SMART 5 min	forward	1.139	23.31	0.76	20.2
	backward	1.137	23.32	0.76	20.2
SMART 30 min	forward	1.145	23.56	0.77	20.8
	backward	1.146	23.62	0.77	20.8
SMART 60 min	forward	1.153	23.78	0.78	21.4
	backward	1.153	23.76	0.78	21.4

https://dx.doi.org/10.1021/acsenergylett.0c02578
ACS Energy Lett. XXXX, XXX, XXX–XXX

example, the cell made with standard perovskite film and annealed for 5 min is denoted "standard 5 min."

For the devices fabricated with the standard perovskite thin films, the "standard 1 min" cell has a power conversion efficiency (PCE) of 11.2% with an open-circuit voltage (V_{oc}) of 1.01 V in backward scan (scan from open circuit to short circuit); using the perovskite film with 5 and 30 min annealing, the cell performance improved significantly to 14.8% and 17.5%, mainly due to an increase in short-circuit current density (J_{sc}) and V_{oc}; and using the perovskite film with 60 min annealing, the cell PCE further increased to 19.3%. The annealing substantially increases the cell efficiency and results in a smaller hysteresis. For the SMART cell group, the 1 min cells already have an efficiency of 18.7%, which is a little lower than the 60 min-annealed standard cells. While the 5 min cells have an efficiency of 20.2%, which is higher than the 60 min-annealed standard cells, and there is no hysteresis for the SMART samples. Further annealing of the SMART films continues to improve the cell performance to 21.4% without hysteresis, but improvements are not as dramatic as in the standard cell group. The SMART perovskite films do have lower defect density, higher carrier mobility, and longer lifetime, which according to references is expected to result in reduced (or more negligible) hysteresis.[41,42] The integrated current densities estimated from the external quantum efficiency (EQE) spectra (Figure S11) of the corresponding devices are in good agreement with the J_{sc} values obtained from the $J-V$ curves. In addition, we compared the different annealing time conditions of our previous self-seeding growth (SSG) process[33] and found that we can only get about 18% at 5 min and cannot get the 20% until 60 min (Figure S12). We also tested the devices based on active area of 0.6 cm^2 (Figure S13) and found that the performance of devices based on SMART 60 min are almost the same; however, the performance of devices based on standard 60 min have a large variation, indicating the higher quality of SMART films is more uniform. In addition, we made the modules of 2 in. × 3 in. (Figure S14), and we got the improved performance of different active areas when just using the spin-coated perovskite precursor without any optimization for the blade-coating. The cell performance enhancement for the SMART films is mainly due to J_{sc} and fill factor (FF) improvements. The J_{sc} in a solar cell is determined by three factors: light-harvesting efficiency (η_{lh}); charge injection/transfer efficiency (η_{inj}); and charge collection efficiency (η_{cc}).[43] We ascribed the improvement of J_{sc} based on SMART perovskite mainly to improved light-harvesting efficiency (Figure S15), decreased SRV, longer lifetime, and longer carrier diffusion length. Also, from the SEM images (Figure S4), we can see the standard cell may have multiple grains from bottom to the top. Although the SMART cell mostly has one grain through the whole perovskite film, grain boundaries on this vertical direction are expected to hinder the carrier transport. FF can be related to V_{oc} and the ideality factor n, which is a measure of junction quality and type of recombination.[44] Hence, the improved FF of SMART cells can be explained by less defects in the perovskite film and lower recombination rate at the interfaces.

To evaluate junction quality and study the charge separation and transport process, we further employed cross-sectional KPFM to scan the interfaces of the standard and SMART cells. By applying a bias voltage to the devices during the measurement, we can resolve the voltage drop across the cross-sectional surface of the cleaved solar cells. The local voltage drop is determined by the equivalent resistance of different layers and interfaces, which is related to the junction quality.[45] Figure 5c–f showed the results of the electrical potential and field profiling from 5 and 60 min devices from the standard and SMART samples. In the cross-sectional KPFM measurement, we averaged the potential profiles under various bias voltages. Then, the "potential difference" curves are those biased profiles with the 0-V profile subtracted, so that the effects of static surface charges can mostly be eliminated. Finally, by numerically calculating the derivative of the potential change, we obtain how the electric field changes across the device stack.

In the "electric-field difference" curves, we observed a dominant electric-field peak at the ETM/perovskite interface and a smaller peak at the perovskite/HTM interface. The electric-field profile throughout the perovskite layer is near zero, and the best-performing cell (SMART 60 min, shown in Figure 5f) has only one peak at the ETM/perovskite interface. This electric-field distribution indicates that these cells have a $p-n$ junction-like structure at the ETM/perovskite interface,[45,46] similar to the polycrystalline inorganic solar cells such as CdTe and $Cu(In,Ga)Se_2$. For the device having this junction-like structure at the front (i.e., light-incident) interface, the other interface at perovskite/HTM acts like a barrier; voltage drop across the interface would be harmful for the device. Because the electric current through the whole device stack must be even, the potential drop and the strength of the electric-field difference across the device are determined by the competition between the voltages needed for a balanced extraction of carriers across the interfaces. Although the ETM/perovskite interface may be different in the standard and SMART cells, we normalized the ETM/perovskite peak to compare the "back-contact" quality at the perovskite/HTM interfaces between these devices. In the standard cell group, the 60 min device (Figure 5d) has a significantly smaller perovskite/HTM peak than the 5 min devices (Figure 5c). The SMART cell group showed a smaller perovskite/HTM peak (Figure 5e,f) than the standard 60 min cell (Figure 5d). In this $p-n$ junction-like case, a large perovskite/HTM peak indicates a small equivalent resistance due to the leaky junction. A smaller perovskite/HTM peak indicates a better back-contact quality that decreases the energy loss for the majority-carrier transport over the interface. This observation is consistent with Figures 3 and 4, where the surface defect and SRV are substantially different in standard and SMART perovskite, and also affects the subsequent HTM deposition and the perovskite/HTM interface.

By using seed modulation to control the perovskite nucleation and growth, we show a faster formation time and better resulting material quality of samples made with the SMART process compared with standard samples made by the conventional "one-step" method. XRD results indicated that the perovskite phase can be formed in a short annealing time of 5 min with high crystallinity. The in situ surface-potential mappings and transient reflection spectroscopy profiles imply that surface or subsurface defects play a dominant role in film electrical properties. The film characteristics were also reflected in device performance, as well as the perovskite/HTM interface quality. The SMART process provides a new pathway for facile high-quality perovskite fabrication, and a widened annealing window allows a large tolerance for processing, which could be beneficial for further large-area and high-volume fabrication with high uniformity.

https://dx.doi.org/10.1021/acsenergylett.0c02578
ACS Energy Lett. XXXX, XXX, XXX−XXX

■ ASSOCIATED CONTENT

Supporting Information

The Supporting Information is available free of charge at https://pubs.acs.org/doi/10.1021/acsenergylett.0c02578.

Experimental section and additional characterization (PDF)

■ AUTHOR INFORMATION

Corresponding Authors

Fei Zhang − *Materials Chemical and Computational Science Directorate, National Renewable Energy Laboratory, Golden, Colorado 80401, United States;* orcid.org/0000-0002-3774-9520; Email: Fei.Zhang@nrel.gov

Chun-Sheng Jiang − *Materials Chemical and Computational Science Directorate, National Renewable Energy Laboratory, Golden, Colorado 80401, United States;* orcid.org/0000-0003-0230-7500; Email: chun.sheng.jiang@nrel.gov

Kai Zhu − *Materials Chemical and Computational Science Directorate, National Renewable Energy Laboratory, Golden, Colorado 80401, United States;* orcid.org/0000-0003-0908-3909; Email: Kai.Zhu@nrel.gov

Authors

Chuanxiao Xiao − *Materials Chemical and Computational Science Directorate, National Renewable Energy Laboratory, Golden, Colorado 80401, United States*

Xihan Chen − *Materials Chemical and Computational Science Directorate, National Renewable Energy Laboratory, Golden, Colorado 80401, United States;* orcid.org/0000-0001-7907-2549

Mengjin Yang − *Materials Chemical and Computational Science Directorate, National Renewable Energy Laboratory, Golden, Colorado 80401, United States*

Steven P. Harvey − *Materials Chemical and Computational Science Directorate, National Renewable Energy Laboratory, Golden, Colorado 80401, United States;* orcid.org/0000-0001-6120-7062

Matthew C. Beard − *Materials Chemical and Computational Science Directorate, National Renewable Energy Laboratory, Golden, Colorado 80401, United States;* orcid.org/0000-0002-2711-1355

Joseph J. Berry − *Materials Chemical and Computational Science Directorate, National Renewable Energy Laboratory, Golden, Colorado 80401, United States*

Mowafak M. Al-Jassim − *Materials Chemical and Computational Science Directorate, National Renewable Energy Laboratory, Golden, Colorado 80401, United States*

Complete contact information is available at: https://pubs.acs.org/10.1021/acsenergylett.0c02578

Author Contributions

†(C.X., F.Z., X.C.) These authors contributed equally.

Notes

The authors declare no competing financial interest.

■ ACKNOWLEDGMENTS

This work was authored by the National Renewable Energy Laboratory, operated by Alliance for Sustainable Energy, LLC, for the U.S. Department of Energy (DOE) under Contract No. DE-AC36-08GO28308. Funding was provided by U.S. Department of Energy Office of Energy Efficiency and Renewable Energy Solar Energy Technologies Office. We acknowledge the support on understanding of transport, recombination, and other optoelectronic properties from the Center for Hybrid Organic Inorganic Semiconductors for Energy (CHOISE), an Energy Frontier Research Center funded by the DOE Office of Basic Energy Sciences, Office of Science; and the support on perovskite synthesis and device fabrication/characterization from the De-Risking Halide Perovskite Solar Cells program of the National Center for Photovoltaics, funded by the U.S. Department of Energy, Office of Energy Efficiency and Renewable Energy, Solar Energy Technologies Office. The views expressed in the article do not necessarily represent the views of the DOE or the U.S. Government. The U.S. Government retains and the publisher, by accepting the article for publication, acknowledges that the U.S. Government retains a nonexclusive, paid-up, irrevocable, worldwide license to publish or reproduce the published form of this work, or allow others to do so, for U.S. Government purposes.

■ REFERENCES

(1) Best Research-Cell Efficiency Chart | Photovoltaic Research | NREL. https://www.nrel.gov/pv/cell-efficiency.html (accessed August, 2020).

(2) Li, Z.; Klein, T. R.; Kim, D. H.; Yang, M.; Berry, J. J.; van Hest, M. F. A. M.; Zhu, K. Scalable Fabrication of Perovskite Solar Cells. *Nat. Rev. Mater.* **2018**, *3* (4), 18017.

(3) De Wolf, S.; Holovsky, J.; Moon, S.-J.; Loper, P.; Niesen, B.; Ledinsky, M.; Haug, F.-J.; Yum, J.-H.; Ballif, C. Organometallic Halide Perovskites: Sharp Optical Absorption Edge and Its Relation to Photovoltaic Performance. *J. Phys. Chem. Lett.* **2014**, *5* (6), 1035−1039.

(4) Yang, Y.; Yang, M.; Li, Z.; Crisp, R.; Zhu, K.; Beard, M. C. Comparison of Recombination Dynamics in CH3NH3PbBr3 and CH3NH3PbI3 Perovskite Films: Influence of Exciton Binding Energy. *J. Phys. Chem. Lett.* **2015**, *6* (23), 4688−4692.

(5) Manser, J. S.; Christians, J. A.; Kamat, P. V. Intriguing Optoelectronic Properties of Metal Halide Perovskites. *Chem. Rev.* **2016**, *116* (21), 12956−13008.

(6) Chen, X.; Lu, H.; Yang, Y.; Beard, M. C. Excitonic Effects in Methylammonium Lead Halide Perovskites. *J. Phys. Chem. Lett.* **2018**, *9* (10), 2595−2603.

(7) Xing, G.; Mathews, N.; Sun, S.; Lim, S. S.; Lam, Y. M.; Gratzel, M.; Mhaisalkar, S.; Sum, T. C. Long-Range Balanced Electron- and Hole-Transport Lengths in Organic-Inorganic CH3NH3PbI3. *Science* **2013**, *342* (6156), 344−347.

(8) Zhai, Y.; Wang, K.; Zhang, F.; Xiao, C.; Rose, A. H.; Zhu, K.; Beard, M. C. Individual Electron and Hole Mobilities in Lead-Halide Perovskites Revealed by Noncontact Methods. *ACS Energy Lett.* **2020**, *5* (1), 47−55.

(9) Tan, H.; Che, F.; Wei, M.; Zhao, Y.; Saidaminov, M. I.; Todorovic, P.; Broberg, D.; Walters, G.; Tan, F.; Zhuang, T.; Sun, B.; Liang, Z.; Yuan, H.; Fron, E.; Kim, J.; Yang, Z.; Voznyy, O.; Asta, M.; Sargent, E. H. Dipolar Cations Confer Defect Tolerance in Wide-Bandgap Metal Halide Perovskites. *Nat. Commun.* **2018**, *9* (1), 3100.

(10) Steirer, K. X.; Schulz, P.; Teeter, G.; Stevanovic, V.; Yang, M.; Zhu, K.; Berry, J. J. Defect Tolerance in Methylammonium Lead Triiodide Perovskite. *ACS Energy Lett.* **2016**, *1* (2), 360−366.

(11) Yin, W.-J.; Shi, T.; Yan, Y. Unique Properties of Halide Perovskites as Possible Origins of the Superior Solar Cell Performance. *Adv. Mater.* **2014**, *26* (27), 4653−4658.

(12) Zhou, Y.; Game, O. S.; Pang, S.; Padture, N. P. Microstructures of Organometal Trihalide Perovskites for Solar Cells: Their Evolution from Solutions and Characterization. *J. Phys. Chem. Lett.* **2015**, *6* (23), 4827−4839.

(13) Aguiar, J. A.; Wozny, S.; Holesinger, T. G.; Aoki, T.; Patel, M. K.; Yang, M.; Berry, J. J.; Al-Jassim, M.; Zhou, W.; Zhu, K. In Situ Investigation of the Formation and Metastability of Formamidinium

Lead Tri-Iodide Perovskite Solar Cells. *Energy Environ. Sci.* **2016**, *9* (7), 2372−2382.
(14) Ro, H. W.; Downing, J. M.; Engmann, S.; Herzing, A. A.; DeLongchamp, D. M.; Richter, L. J.; Mukherjee, S.; Ade, H.; Abdelsamie, M.; Jagadamma, L. K.; Amassian, A.; Liu, Y.; Yan, H. Morphology Changes upon Scaling a High-Efficiency, Solution-Processed Solar Cell. *Energy Environ. Sci.* **2016**, *9* (9), 2835−2846.
(15) Ke, W.; Xiao, C.; Wang, C.; Saparov, B.; Duan, H.-S.; Zhao, D.; Xiao, Z.; Schulz, P.; Harvey, S. P.; Liao, W.; Meng, W.; Yu, Y.; Cimaroli, A. J.; Jiang, C.-S.; Zhu, K.; Al-Jassim, M.; Fang, G.; Mitzi, D. B.; Yan, Y. Employing Lead Thiocyanate Additive to Reduce the Hysteresis and Boost the Fill Factor of Planar Perovskite Solar Cells. *Adv. Mater.* **2016**, *28* (26), 5214−5221.
(16) Hu, Q.; Zhao, L.; Wu, J.; Gao, K.; Luo, D.; Jiang, Y.; Zhang, Z.; Zhu, C.; Schaible, E.; Hexemer, A.; Wang, C.; Liu, Y.; Zhang, W.; Gratzel, M.; Liu, F.; Russell, T. P.; Zhu, R.; Gong, Q. In Situ Dynamic Observations of Perovskite Crystallisation and Microstructure Evolution Intermediated from [PbI 6] 4− Cage Nanoparticles. *Nat. Commun.* **2017**, *8* (1), 15688.
(17) Jung, M.; Ji, S.-G.; Kim, G.; Seok, S. I. Perovskite Precursor Solution Chemistry: From Fundamentals to Photovoltaic Applications. *Chem. Soc. Rev.* **2019**, *48* (7), 2011−2038.
(18) Jeon, N. J.; Noh, J. H.; Kim, Y. C.; Yang, W. S.; Ryu, S.; Seok, S. I. Solvent Engineering for High-Performance Inorganic−Organic Hybrid Perovskite Solar Cells. *Nat. Mater.* **2014**, *13* (9), 897−903.
(19) Park, N.-G.; Zhu, K. Scalable Fabrication and Coating Methods for Perovskite Solar Cells and Solar Modules. *Nat. Rev. Mater.* **2020**, *5*, 333−350.
(20) Yang, M.; Li, Z.; Reese, M. O.; Reid, O. G.; Kim, D. H.; Siol, S.; Klein, T. R.; Yan, Y.; Berry, J. J.; van Hest, M. F. A. M.; Zhu, K. Perovskite Ink with Wide Processing Window for Scalable High-Efficiency Solar Cells. *Nat. Energy* **2017**, *2* (5), 1−9.
(21) Jiang, Y.; Leyden, M. R.; Qiu, L.; Wang, S.; Ono, L. K.; Wu, Z.; Juarez-Perez, E. J.; Qi, Y. Combination of Hybrid CVD and Cation Exchange for Upscaling Cs-Substituted Mixed Cation Perovskite Solar Cells with High Efficiency and Stability. *Adv. Funct. Mater.* **2018**, *28* (1), 1703835.
(22) Bi, D.; Yi, C.; Luo, J.; Decoppet, J.-D.; Zhang, F.; Zakeeruddin, S. M.; Li, X.; Hagfeldt, A.; Gratzel, M. Polymer-Templated Nucleation and Crystal Growth of Perovskite Films for Solar Cells with Efficiency Greater than 21%. *Nat. Energy* **2016**, *1* (10), 1−5.
(23) Min, H.; Kim, M.; Lee, S.-U.; Kim, H.; Kim, G.; Choi, K.; Lee, J. H.; Seok, S. I. Efficient, Stable Solar Cells by Using Inherent Bandgap of α-Phase Formamidinium Lead Iodide. *Science* **2019**, *366* (6466), 749−753.
(24) Jung, E. H.; Jeon, N. J.; Park, E. Y.; Moon, C. S.; Shin, T. J.; Yang, T.-Y.; Noh, J. H.; Seo, J. Efficient, Stable and Scalable Perovskite Solar Cells Using Poly(3-Hexylthiophene). *Nature* **2019**, *567* (7749), 511−515.
(25) Kim, M.; Kim, G.-H.; Lee, T. K.; Choi, I. W.; Choi, H. W.; Jo, Y.; Yoon, Y. J.; Kim, J. W.; Lee, J.; Huh, D.; Lee, H.; Kwak, S. K.; Kim, J. Y.; Kim, D. S. Methylammonium Chloride Induces Intermediate Phase Stabilization for Efficient Perovskite Solar Cells. *Joule* **2019**, *3* (9), 2179−2192.
(26) Zhu, H.; Liu, Y.; Eickemeyer, F. T.; Pan, L.; Ren, D.; Ruiz-Preciado, M. A.; Carlsen, B.; Yang, B.; Dong, X.; Wang, Z.; Liu, H.; Wang, S.; Zakeeruddin, S. M.; Hagfeldt, A.; Dar, M. I.; Li, X.; Gratzel, M. Tailored Amphiphilic Molecular Mitigators for Stable Perovskite Solar Cells with 23.5% Efficiency. *Adv. Mater.* **2020**, *32* (12), 1907757.
(27) Malinkiewicz, O.; Yella, A.; Lee, Y. H.; Espallargas, G. M.; Graetzel, M.; Nazeeruddin, M. K.; Bolink, H. J. Perovskite Solar Cells Employing Organic Charge-Transport Layers. *Nat. Photonics* **2014**, *8* (2), 128−132.
(28) Ono, L. K.; Wang, S.; Kato, Y.; Raga, S. R.; Qi, Y. Fabrication of Semi-Transparent Perovskite Films with Centimeter-Scale Superior Uniformity by the Hybrid Deposition Method. *Energy Environ. Sci.* **2014**, *7* (12), 3989−3993.
(29) Qiu, L.; He, S.; Liu, Z.; Ono, L. K.; Son, D.-Y.; Liu, Y.; Tong, G.; Qi, Y. Rapid Hybrid Chemical Vapor Deposition for Efficient and Hysteresis-Free Perovskite Solar Modules with an Operation Lifetime Exceeding 800 h. *J. Mater. Chem. A* **2020**, *8* (44), 23404−23412.
(30) Sanchez, S.; Jeronimo-Rendon, J.; Saliba, M.; Hagfeldt, A. Highly Efficient and Rapid Manufactured Perovskite Solar Cells via Flash InfraRed Annealing. *Mater. Today* **2020**, *35*, 9−15.
(31) Stoddard, N.; Wu, B.; Witting, I.; Wagener, M. C.; Park, Y.; Rozgonyi, G. A.; Clark, R. Casting Single Crystal Silicon: Novel Defect Profiles from BP Solar's Mono$^{2\ TM}$ Wafers. In *Solid State Phenomena*, Vol. *131−133*; Cavallini, A., Richter, H., Kittler, M., Pizzini, S., Eds.; Trans Tech Publications, Ltd., 2007. DOI: 10.4028/www.scientific.net/SSP.131-133.1.
(32) Wang, P.; Cui, C.; Yang, D.; Yu, X. Seed-Assisted Growth of Cast-Mono Silicon for Photovoltaic Application: Challenges and Strategies. *Sol. RRL* **2020**, *4* (5), 1900486.
(33) Zhang, F.; Xiao, C.; Chen, X.; Larson, B. W.; Harvey, S. P.; Berry, J. J.; Zhu, K. Self-Seeding Growth for Perovskite Solar Cells with Enhanced Stability. *Joule* **2019**, *3* (6), 1452−1463.
(34) Zhang, Y.; Seo, S.; Lim, S. Y.; Kim, Y.; Kim, S.-G.; Lee, D.-K.; Lee, S.-H.; Shin, H.; Cheong, H.; Park, N.-G. Achieving Reproducible and High-Efficiency (>21%) Perovskite Solar Cells with a Presynthesized FAPbI3 Powder. *ACS Energy Lett.* **2020**, *5* (2), 360−366.
(35) Schelhas, L. T.; Li, Z.; Christians, J. A.; Goyal, A.; Kairys, P.; Harvey, S. P.; Kim, D. H.; Stone, K. H.; Luther, J. M.; Zhu, K.; Stevanovic, V.; Berry, J. J. Insights into Operational Stability and Processing of Halide Perovskite Active Layers. *Energy Environ. Sci.* **2019**, *12* (4), 1341−1348.
(36) Xiao, C.; Jiang, C.-S.; Johnston, S.; Yang, X.; Ye, J.; Gorman, B.; Al-Jassim, M. Development of In-Situ High-Voltage and High-Temperature Stressing Capability on Atomic Force Microscopy Platform. *Sol. Energy* **2017**, *158*, 746−752.
(37) Chen, C.; Song, Z.; Xiao, C.; Zhao, D.; Shrestha, N.; Li, C.; Yang, G.; Yao, F.; Zheng, X.; Ellingson, R. J.; Jiang, C.-S.; Al-Jassim, M.; Zhu, K.; Fang, G.; Yan, Y. Achieving a High Open-Circuit Voltage in Inverted Wide-Bandgap Perovskite Solar Cells with a Graded Perovskite Homojunction. *Nano Energy* **2019**, *61*, 141−147.
(38) Wang, R.; Xue, J.; Wang, K.-L.; Wang, Z.-K.; Luo, Y.; Fenning, D.; Xu, G.; Nuryyeva, S.; Huang, T.; Zhao, Y.; Yang, J. L.; Zhu, J.; Wang, M.; Tan, S.; Yavuz, I.; Houk, K. N.; Yang, Y. Constructive Molecular Configurations for Surface-Defect Passivation of Perovskite Photovoltaics. *Science* **2019**, *366* (6472), 1509−1513.
(39) Xiao, C.; Zhang, F.; Li, Z.; Harvey, S. P.; Chen, X.; Wang, K.; Jiang, C.-S.; Zhu, K.; Al-Jassim, M. Inhomogeneous Doping of Perovskite Materials by Dopants from Hole-Transport Layer. *Matter* **2020**, *2* (1), 261−272.
(40) Chen, X.; Wang, K.; Beard, M. C. Ultrafast Probes at the Interfaces of Solar Energy Conversion Materials. *Phys. Chem. Chem. Phys.* **2019**, *21* (30), 16399−16407.
(41) Elumalai, N. K.; Uddin, A. Hysteresis in Organic-Inorganic Hybrid Perovskite Solar Cells. *Sol. Energy Mater. Sol. Cells* **2016**, *157*, 476−509.
(42) Yuan, Y.; Huang, J. Ion Migration in Organometal Trihalide Perovskite and Its Impact on Photovoltaic Efficiency and Stability. *Acc. Chem. Res.* **2016**, *49* (2), 286−293.
(43) Chiang, C.-H.; Wu, C.-G. Bulk Heterojunction Perovskite−PCBM Solar Cells with High Fill Factor. *Nat. Photonics* **2016**, *10* (3), 196−200.
(44) Green, M. A. Solar Cell Fill Factors: General Graph and Empirical Expressions. *Solid-State Electron.* **1981**, *24* (8), 788−789.
(45) Xiao, C.; Wang, C.; Ke, W.; Gorman, B. P.; Ye, J.; Jiang, C.-S.; Yan, Y.; Al-Jassim, M. M. Junction Quality of SnO2-Based Perovskite Solar Cells Investigated by Nanometer-Scale Electrical Potential Profiling. *ACS Appl. Mater. Interfaces* **2017**, *9* (44), 38373−38380.
(46) Jiang, C.-S.; Yang, M.; Zhou, Y.; To, B.; Nanayakkara, S. U.; Luther, J. M.; Zhou, W.; Berry, J. J.; van de Lagemaat, J.; Padture, N. P.; Zhu, K.; Al-Jassim, M. M. Carrier Separation and Transport in

https://dx.doi.org/10.1021/acsenergylett.0c02578
ACS Energy Lett. XXXX, XXX, XXX−XXX

726 Perovskite Solar Cells Studied by Nanometre-Scale Profiling of
727 Electrical Potential. *Nat. Commun.* **2015**, *6*, 8397.

https://dx.doi.org/10.1021/acsenergylett.0c02578
ACS Energy Lett. XXXX, XXX, XXX−XXX